Supporting Information

Supercapacitor with ultrahigh volumetric capacitance produced by self-assembly of reduced graphene oxide through phosphoric acid treatment

Zhaoyuan Liu,[a] Lidong Wang,*[a] Guizhi Ma,[a] Yinan Yuan,[a] Henan Jia,[a] Weidong Fei*[ab]

[a]*School of Materials Science and Engineering, Harbin Institute of Technology, Harbin 150001, P. R. China. E-mail: wld@hit.edu.cn, wdfei@hit.edu.cn*

[b]*State Key Laboratory of Advanced Welding and Joining, Harbin Institute of Technology, Harbin 150001, P. R. China.*

Experimental section

Synthesis of materials: Graphite oxide was synthesized using a modified Hummers method [1]. Natural graphite powder with an average size of 44 μm was purchased from Qingdao Jinrilai Graphite Co., Ltd. Briefly, a volume ratio of 9:1 mixture of concentrated H_2SO_4 (98%, 90 mL) and H_3PO_4 (85%, 10 mL) was added to the nature graphite powder (2 g) in ice-water bath. $KMnO_4$ (14 g) was gradually added with magnetic stirring, then the reactants were heated to 50 °C and stirred for 10 h. The reactants were cooled down to room temperature and distilled water (50 mL) was slowly added to cause an increase in temperature up to 95 °C, holding for 15 min and then a large amount of distilled water (450 mL) and 30% H_2O_2 solution (5 mL) were added to the reaction system. The product was washed by diluted hydrochloric acid and deionized water for several times. The GO colloid solution was freeze-dried for 48 h and denoted as GO-Or.

GO suspension (2 mg mL^{-1}, 600 mL) was treated by sonication for 2 h and then mixed with concentrated H_3PO_4 (85%, 400 mL) and stirring for 30 min. The mixture was divided into four parts and three of them were put into a household microwave oven (Galanz, 700W) and microwaved for 30, 40 and 50 min, respectively, and then washed with deionized water until the pH of the washed water became neutral; the samples were finally freeze-dried for 48 h and denoted as RGO-MPX (X = 30, 40, 50), in which X refers to their microwave treatment time. As a comparison, GO powder heated in a tubular furnace in argon with the same temperature-rising curve of RGO-MP40 is designated as RGO-H40. In addition, we added another control experiment: the mixture of H_3PO_4 and GO was directly heated to the same temperature with RGO-MP40 in a round-bottom flask with a heating jacket (250 mL, 180 W) and the obtained sample was denoted as RGO-P40. Another control sample was also set as microwave assisted reduction of graphene oxide with enough deionized water and denoted as RGO-M40. The temperature of the sample after microwave was measured by an infrared thermometer (Pro'sKit,

MT-4003) with an accuracy of ±2%. Ones should note that it's inappropriate to set the control group as microwave assisted reduction of graphene oxide without phosphoric acid. When the water is completely removed out, graphene oxide will experience an extremely fast annealing process upon the microwave irradiation and the GO will be heated up to thousands of Celsius in only few of milliseconds, so it is difficult to strictly control the temperature of this control group.

Characterizations: The microstructure and morphology were examined by environmental scanning electron microscopy (ESEM, Helios Nanolab 600i) and high-resolution transmission electron microscopy (HRTEM, Tecnai G2 F30). The X-ray photoelectron spectroscopy (XPS) characterization of the products was executed on Thermo Fisher spectrometer with an Al Kα (*hv*=1486.69 eV) X-ray source. The powder X-ray diffraction (XRD) measurements were carried out on a Philips X'pert diffractometer with Cu Kα irradiation (λ=1.54 Å). The Raman spectra were recorded using a B&WTEK spectrometer (BWS435-532SY) with a 532 nm laser (*hv*=2.34 eV), 2% laser power (total power: 240 mW). The FTIR spectra were recorded in KBr pellets using a Perkin Elmer FTIR spectrometer in the wavenumber region 4000 to 400 cm^{-1}. Electrical conductivity was performed by first pressing the samples powder under 10 MPa into a platelet with a thickness of 250 μm, and then measuring this platelet on a four-probe electrical conductivity instrument. The nitrogen adsorption/desorption isotherms were measured using a Quantachrome NOVA 4200 e system. EPR measurements were performed with an EPR X-band (9.85 GHz) spectrometer (Bruker-A300) at room temperature. Following EPR experimental parameters were used: microwave power: 19.15 mW, modulation amplitude: 1.0 G, time constant: 10.24 ms and receiver gain: 1×10^3.

Surface area measurement:

The specific surface area and pore size distribution were determined by Brunauer-Emmett-Teller (BET) and Barrett-Joyner-Halenda (BJH) desorption analyses, respectively. The packing density of RGOs was calculated through the following equation [2, 3]:

$$\rho_m = \left(V_{total} + 1/\rho_{carbon}\right)^{-1} \qquad \text{* MERGEFORMAT (1)}$$

where ρ_m is the particle density of the materials and the ρ_{carbon} is the true density of carbon (2 g cm^{-3}), V_{total} is the total pore volume estimated from N_2 isotherm at 77 K.

Cyclic voltammetry (CV) measurement was used to determine the active surface area with an electrochemical workstation (CHI760E, Chenhua, Shanghai, China) at room temperature, using a conventional three-electrode system consisting of a grassy carbon electrode (diameter = 5 mm), a platinum plate electrode, and an Ag/AgCl electrode as the working electrode, the counter electrode, and the reference electrode, respectively. 100 μg RGO-MP40 and RGO-H40 were uniformly coated on the glassy carbon electrode respectively for the CV tests. A solution of 0.1 M KCl and 10 mM $K_3Fe(CN)_6$ as the electrolyte. The effective surface area can be calculated from the Randles–Sevcik equation:

$$i_p = (2.678\times10^5)n^{3/2}v^{1/2}D^{1/2}AC \qquad \text{* MERGEFORMAT (2)}$$

where i_p refers to the peak current, n is the number of electron transferred in the redox process (n=1, in 10 mM $K_3Fe(CN)_6$), v is the scan rate, D is the diffusion coefficient (D = 5.7 × 10^{-6} cm^2 s^{-1}, in 0.1 M KCl), A is the surface area and C is the concentration of $K_3Fe(CN)_6$.

Electrochemical measurements: The electrochemical experiments were carried out using a conventional three- and two-electrode system with an aqueous system (electrolyte: 1 M H_2SO_4) using CHI760D electrochemical workstation. Three-electrode cells were used to evaluate the Faradaic processes and the available potential window, and two-electrode cells were

constructed to simulate actual device behavior. The working electrode was prepared by mixing the active materials with polyvinylidene fluoride (PVDF) and acetylene black with a weight ratio of 85:10:5 in N-methyl-2-pyrrolidone (NMP) until homogeneous slurry was formed. For mass loading >10 mg cm^{-2}, 10 wt.% PVDF was used to ensure the adhesive strength of the electrode to the current collector. The as-prepared slurry was dropped onto the graphite foil (90 μm, from Qingdao Herita Graphite products Co., Ltd.) with areal of 1 cm^2, with different active mass loading of 2.5 to 19.7 mg cm^{-2}. The electrode was dried at 120 °C in a vacuum oven for 10 h. After then, the electrode was pressed under 10 MPa for 2 minutes to improve the packing density. The typical optical photograph of the graphene electrode RGO-MP40 supported by graphite paper at a mass loading of 2.5 mg cm^{-2} was provide in **Figure S26**. To determine the packing density of the electrode (ρ_e), we calculated the volume by measuring the thickness and the geometric area of the compressed electrode at the mass loading of 12 mg cm^{-2} (**Figure S18**). We thus obtained the packing density by dividing the total electrode mass by the volume of the electrode. The Ag/AgCl ($KCl_{sat.}$) electrode and a slice of platinum served as reference and counter electrodes, respectively. For all the samples, before formally starting the electrochemical test, the activation was performed at the scan rate of 100 mV s^{-1} for 100 cycles to stabilize the electrode. The cyclic voltammetry (CV) tests were investigated between -0.2 and 1.0 V (*vs.* Ag/AgCl). The galvanostatic charge/discharge was performed in the same potential range at the current densities ranging from 0.1 to 50 A g^{-1}. Galvanostatic charge/discharge was assumed to be the most accurate technique especially for redox supercapacitor. The electrochemical impendence spectroscopy (EIS) measurements were evaluated in the frequency range from 100 kHz to 0.01 Hz at open circuit potential with an ac perturbation of 5 mV. The simulation of the experiment impedance using three-electrode data was carried out with Zview software.

Fabrication of supercapacitors: As for the fabrication of the two-electrode symmetric supercapacitor systems, two electrodes with exactly the same mass were assembled in CR2032 stainless steel coin-type cells with the porous cellulose membrane as separator and 1 M H_2SO_4 aqueous solution as electrolyte. The active materials on each electrode was ~20 mg, with the areal density of about 20 mg cm^{-2} and bulk density of about 1.47 g cm^{-3}.

Calculation of the specific capacitances: The measured specific capacitance of the current collector (90 μm graphite foil) with density of 17 mg cm^{-2} is about 1.64 F g^{-1} (**Figure S27**). All of the specific capacitances were corrected by deducting the background capacitance from the graphite paper (**Figure S28**).

(1) Three-electrode configuration

The gravimetric specific capacitances based on the active material ($C_{g\text{-}m}$, F g^{-1}) were calculated according to the curves of constant current charge/discharge at different current densities:

$$C_{g\text{-}m} = \frac{I\Delta t}{m\Delta U} \qquad \text{* MERGEFORMAT (3)}$$

where I is the discharge current (A), Δt is the discharge time (s), m is the weight of the active material (g), and ΔU is the discharge voltage (V) excluding the internal resistance (iR) drop during the discharge process.

The volumetric performances of the active materials ($C_{V\text{-}m}$, F cm^{-3}) were calculated according to the following equation:

$$C_{V\text{-}m} = C_{g\text{-}m}\rho_m \qquad \text{* MERGEFORMAT (4)}$$

where $C_{g\text{-}m}$ presents the gravimetric capacitance of the active material, ρ_m is the packing density (g cm^{-3}) of the active material.

The gravimetric capacitances of electrode ($C_{g\text{-}e}$, F g^{-1}) were calculated by dividing the total

mass of the electrode material (including active material, carbon black and PVDF).

The volumetric capacitance of the electrodes ($C_{V\text{-}e}$) was calculated according to the following equation:

$$C_{V\text{-}e} = C_{g\text{-}e}\rho_e \qquad \text{* MERGEFORMAT (5)}$$

where ρ_e is the electrode density (including the carbon black and PVDF).

The areal specific capacitance ($C_{A\text{-}e}$, F cm^{-2}) is calculated as followed:

$$C_{A\text{-}e} = C_g\rho_A \qquad \text{* MERGEFORMAT (6)}$$

where $C_{A\text{-}e}$ (mF cm^{-2}) and ρ_A (mg cm^{-2}) are geometric areal specific capacitance and the active material mass loading, respectively.

(2) Two-electrode configuration

The gravimetric specific capacitance of the device was calculated by the following equation:

$$C_{g\text{-}2e} = \frac{I\Delta t}{2m\Delta U} \qquad \text{* MERGEFORMAT (7)}$$

where I is the discharge current (A), Δt is the discharge time (s), m is the weight of the active material in the individual electrode (g), and ΔU is the discharge voltage (V) excluding the iR drop during the discharge process.

The volumetric capacitance of the two-electrode system was calculated by the following equation:

$$C_{V\text{-}2e} = \frac{I\Delta t}{2V\Delta U} \qquad \text{* MERGEFORMAT (8)}$$

where I is the discharge current (A), Δt is the discharge time (s), V is the volume of the individual electrode (cm^3), and ΔU is the discharge voltage (V) excluding the iR drop during the discharge process.

The areal specific capacitance of the two-electrode system was calculated by the following equation:

$$C_{A\,2e} = \frac{I\Delta t}{S\Delta U} \qquad \text{* MERGEFORMAT (9)}$$

where I is the discharge current (A), Δt is the discharge time (s), S is the areal of the individual electrode (cm^2), and ΔU is the discharge voltage (V) excluding the iR drop during the discharge process.

The energy densities (E) and power density (P) of the symmetric cell were estimated according to the following equation:

$$E = \frac{1}{2} C \times \Delta U^2 \qquad \text{* MERGEFORMAT (10)}$$

$$P = \frac{E}{t} \qquad \text{* MERGEFORMAT (11)}$$

Where C represents the gravimetric/areal/volumetric capacitance based on the two-electrode system. ΔU is the discharge voltage excluding the iR drop during the discharge process, and t is the discharging time measured in the galvanostatic charging and discharging experiments.

Supplementary Note 1: The defects in GO and RGOs

The nature of defects: The defects in graphene oxide can be divided into two categories: lattice defects corresponding to carbon atoms and defects related to oxygen functional groups. (i) Corrugations, topological defects, adatoms, vacancies, and sp^3-defects are lattice defects [4] that originate from the broken of the C-C bonds which make graphene sheets distorted. These defects can be measured by Raman spectrum and give rise to the D peak. (ii) The defects corresponding to the oxygen functional groups include carboxyl group, carbonyl group, epoxy group, and hydroxyl group, etc., are connected to the graphene layers by covalent bonds and also introduce various edges and defects sites. They are FTIR sensitive defects.

The Raman information shows only one side of the nature of defects. For a more comprehensive analysis of the defects, we also took the XPS and FTIR information into consideration.

The origination of defects: The defects in GO, RGO-MPx, and RGO-H40 were induced during the preparation and heat treatment processes. In the preparation process, GO was produced by improved Hummers method [1]. In the preparation process, flake graphite was oxidized by strong oxidation agents ($KMnO_4$) and concentrated acids (H_2SO_4), thus leading to the rupture of the graphene lattice and forming the latticed defects and oxygen functional groups. In the heat treatment process, the lattice defects were induced by the release of CO and CO_2, which broke the C-C bond and make the graphene sheet distorted [5].

Specifically, different treatment method can lead to different defects. In our phosphorous acid treatment (PAT) process, partial epoxy group (C-O-C) transformed to C-OH group (the result of FTIR and XPS) and subsequently protected by H_3PO_4, thus the elimination of CO_2 and CO was suppressed as the highly strained epoxy groups and the adjacent C-OH are the primary causes for the evolution of CO_2 and CO [6]. As a result, the lattice defect concentration of RGO-MP40 is lower than that of RGO-H40, as indicated by the lower I_D/I_G value of RGO-MP40 than

that of RGO-H40. This is also confirmed by the TEM characteristics where the graphene sheet of RGO-MP40 is very integrated whereas the RGO-H40 generates a lot of holes in the basal plane (**Figure S5**).

The roles of defects. On one hand, the oxygen functional groups could not only improve the wettability but also provide extra pseudocapacitance by C=O/C-OH redox reaction. However, too much oxygen functional groups will make graphene a insulator, such as graphene oxide. So, there is a balance between the oxygen functional groups and the capacitive performance. Nevertheless, this type of defect is favorable for the electrochemistry properties in the case of RGO-MP40. On the other hand, the lattice defects are the scattering center for electron transport, and will decrease electrical conductivity, as in the case of RGO-H40. Thus, this type of defect, to some extent, is not favorable for high capacitive performance.

Supplementary Note 2: Distinguishing between capacitive and diffusion-controlled processes

It is important to analysis the charge storage mechanism. The total storage charge can be separated into three components: the faradic contribution form diffusion-controlled process, the faradic contribution from charge transfer processes in the graphene surfaces referred as redox pseudocapacitance, and the non-faradic contribution from the double layer capacitance. Following the Dunn's method, we are able to use the voltammetric sweep rate dependence to determine quantitatively the capacitive contribution to the current response.

First, the current density, i at a fixed potential and a scan rate, is composed of two terms associated with the scan rate, v:

$$i = \mathrm{k}_1 v + \mathrm{k}_2 v^{0.5} \qquad \text{* MERGEFORMAT (12)}$$

where k_1 and k_2 are the constants. The $\mathrm{k}_1 v$ and $\mathrm{k}_2 v^{0.5}$ equals to the current density contributions from fast-kinetic processes and slow-kinetic (or diffusion-controlled) processes. For analytical purposes, we rearrange equation * MERGEFORMAT (12) by dividing $v^{0.5}$ on both side and

obtain:

$$iv^{-0.5} = k_1 v^{0.5} + k_2 \qquad \text{* MERGEFORMAT (13)}$$

Equation * MERGEFORMAT (13) shows that $iv^{-0.5}$ and $v^{0.5}$ are expected to have a linear relationship with k_1 and k_2 being the slope and y-intercept, respectively. By determining k_1 and k_2, we are able to quantify, at specific potentials, the fraction of the current arising from diffusion-controlled processes and that from the capacitive processes. The results are shown in **Figure S15.**

Supplementary Note 3: Estimation of the contribution of double layer capacitance (C_{dl}) and pseudocapacitance (C_p)

About the calculation of the double layer capacitance (C_{dl}) and pseudocapacitance (C_p), it should be noticed that it is still a great challenge to distinguish the contributions of the electrical double layer (EDL) formation and redox reactions to the total current, owing to complicated kinetic and ohmic drop effects, as well as the sophisticated relationship between the scan-rate and the CV response [7, 8]. Here, we summarized several methods according to the literatures. They are listed below briefly.

Method 1: The charge storage mechanisms of metal oxides can be obtained by simulating CV curves based on the first-principles [7, 9]. However, this method only simulated the situation of two-dimensional (planar) electrode. In addition, the simplified geometry of the device and the assumptions during the simulating process make the model far from the actual experimental conditions.

Method 2: For porous Electrodes (Ag, Ni and carbon), a modified triangular voltage sweep (TVS) was used to determine C_{dl} by eliminating the Faradaic currents and distributed capacity [10-13]. However, it could only determine C_{dl}, and when both faradaic current and distributed capacity effects are significant, it is difficult to handle mathematically. In addition, the theory does not consider the physical and chemical nature of faradaic capacity and

distributed capacity, so it cannot distinguish the difference between the above two.

Method 3: For porous graphene sheets, the C_{dl} and C_p were evaluated by capacitances of the material before and after removing surface functionality by heat treatment [3]. By deducting the capacitance of the high temperature treatment materials (mainly C_{dl}) from the total capacitance, C_p from the oxygen functional groups can be obtained. However, for our layered RGO material with high packing density, the high temperature heat treatment would alter its surface chemical properties and make it hydrophobic, which deteriorates its double layer capacitive performance. So, this method is not suitable for our RGO material.

Method 4: The C_p and C_{dl} are evaluated by comparing the capacitances in acidic, basic and non-aqueous media [14, 15]. Since the electrochemical signature of C_p in different electrolytic media is complicated, and replacing electrolyte would also influence the behavior of double layer capacitance as C_{dl} is related with the hydration or solvation radius of ions. Thus, this method also has obvious deficiency in distinguishing the C_{dl} and C_p.

Method 5: The C_{dl} of carbon felt was measured by CV technique in a specific short potential range where there is no contribution of pseudocapacitance from surface functional groups [16]. In our case, it is practical to find a potential range for pure double layer in the CV curves, since the main reaction for our RGO-MP40 electrode is the redox reaction between the C–OH and C=O groups with a midpoint potential of ~0.4 V *vs*. Ag/AgCl.

In this manuscript, In this manuscript, we estimated the C_{dl} based on method 5 and the experimental data. Firstly, CV test of RGO-MP40 was carried out at different voltage windows (from -0.2~-0.1V to -0.2~1.0V with a step of 0.1 V) as shown in **Figure S16a**. By calculating the specific capacitances at different operating voltages, we found that the capacitance remained basically the same when the upper limit of the potential scan is higher than 0.7 V (**Figure S16b**). This indicates that the redox reaction has completed and the charge storage mechanism is mainly electrical double layer after 0.7 V. In addition, there are no known redox reactions in

the potential range of 0.8~0.9 V. Based on these considerations, we selected the potential range of 0.8~0.9 V to determine the C_{dl} by CV at 5 mV s^{-1}. The schematic illustrations of C_{dl} of RGO-MP40 and RGO-H40 are shown in **Figure S16c** and **d**, respectively. The yellow area in **Figure S16c** is related to the faradaic current corresponding to the broaden of redox peaks, commonly observed for redox action controlled by mass transfer [17]. For CV curve measured at in the potential range of 0.8~0.9 V, faradaic current is eliminated, and the C_{dl} can be calculated according to the area of the CV curves plotted by the red solid line. The contribution of C_p can be obtained by deducting the C_{dl} from the capacitive contribution measured by Dunn's method (Supplementary Note 2).

Supplementary Note 4: The discussion of the time constant

We can define

$$C(\omega) = C'(\omega) - jC''(\omega) \qquad \text{* MERGEFORMAT (14)}$$

leading to

$$C'(\omega) = \frac{-Z''(\omega)}{\omega\left|Z(\omega)\right|^2} \qquad \text{* MERGEFORMAT (15)}$$

$$C''(\omega) = \frac{Z'(\omega)}{\omega\left|Z(\omega)\right|^2} \qquad \text{* MERGEFORMAT (16)}$$

where $C'(\omega)$ is the real part of the capacitance $C(\omega)$. The low frequency value of $C'(\omega)$ corresponds to the capacitance of the cell that is measured during constant current discharge, for example. $C''(\omega)$ is the imaginary part of the capacitance $C(\omega)$. It corresponds to an energy dissipation by an irreversible process that can lead to a hysteresis.

At the characteristic frequency point $\omega_0=2\pi f_0$, according to the relationship of $-Z'(\omega_0)=Z''(\omega_0)$, $-C'(\omega_0)=C''(\omega_0)$, we can obtain the time constant τ_0,

$$\tau_0=\frac{1}{f_0}=4\pi C'(\omega_0)Z'(\omega_0) \qquad \text{* MERGEFORMAT (17)}$$

According to equation * MERGEFORMAT (17), it is not a strange thing that the smaller resistance leads to the slower response time. At the characteristic frequency point, the real parts of the capacitance are 0.337 F and 0.077 F for RGO-MP40 and RGO-H40, respectively; and the real parts of impedance Z' are 1.61 Ω and 2.68 Ω for RGO-MP40 and RGO-H40, respectively (**Figure S21b and c**). Larger capacitance will need longer time to obtain the specific voltage for the capacitor, though the ESR of RGO-MP40 is smaller than that of RGO-H40. Compared with RGO-H40, the larger capacitance of RGO-MP40 is due to the pseudocapacitance contribution from the redox reaction of quinone and hydroquinone at 0.4 V under which we carried out our EIS experiment. This meant that the larger of the capacitance, the longer time it takes for the charge through the given resistance. Therefore, combined with these two respects, based on smaller R and larger C, the frequency response time of RGO-MP40 is slower than that of RGO-H40.

Supplementary Figures S1-S28 and Tables S1-S5

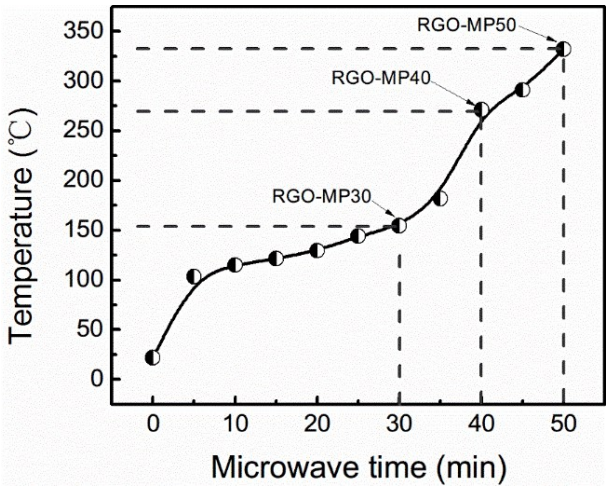

Figure S1 The temperature increasing curve during the microwave treatment process.

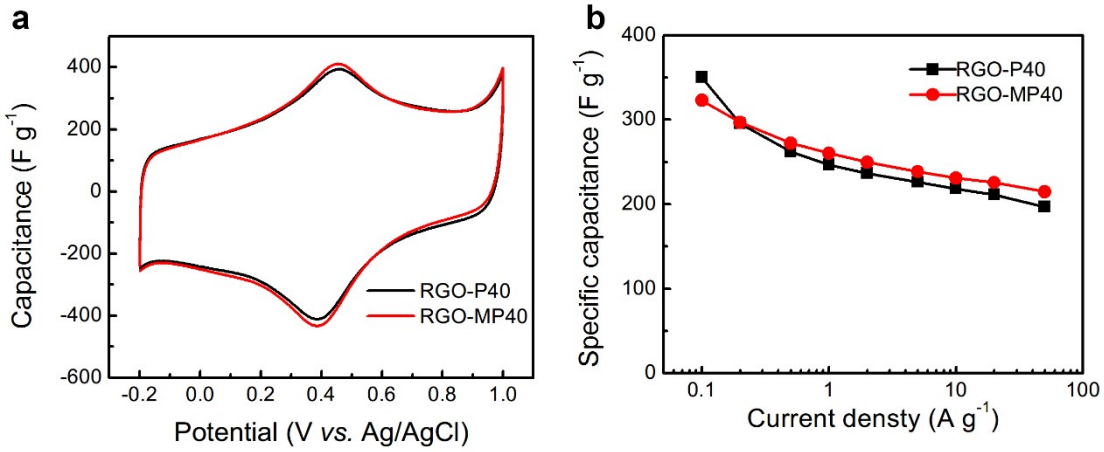

Figure S2 Comparison of the electrochemical properties of RGO-MP40 and RGO-P40 with a similar mass loading of 2.5 mg cm^{-2}. (**a**) The CV curves of the two samples at 5 mV s^{-1}. (**b**) The gravimetric specific capacitance versus different current density from 0.1 to 50 A g^{-1}.

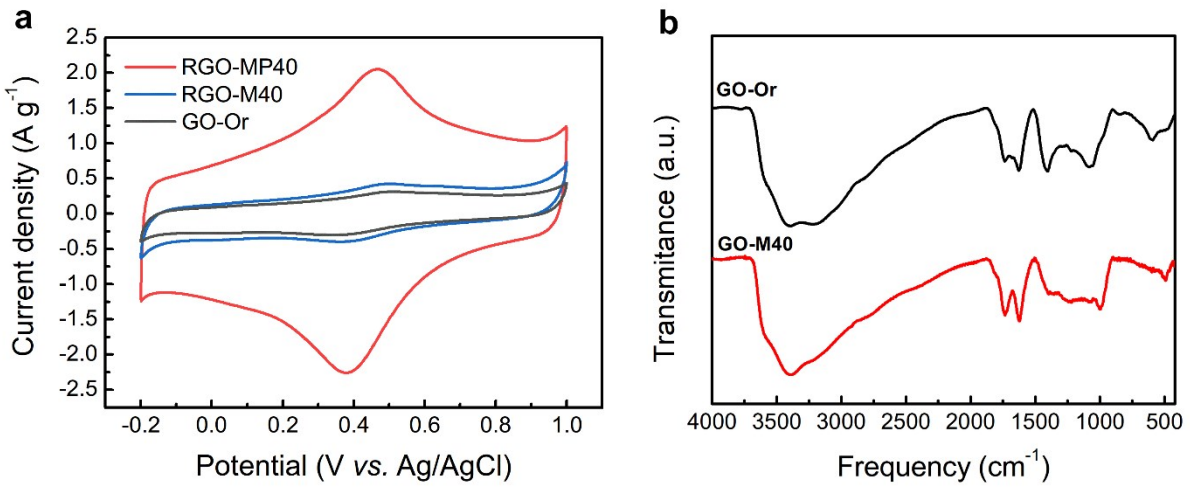

Figure S3 (a) Comparison of the electrochemical properties of RGO-MP40, RGO-M40 and GO-Or with a similar mass loading (5.2 mg cm^{-2} for RGO-MP40, 5.8 mg cm^{-2} for RGO-M40 and 8.2 mg cm^{-2} for GO-Or). (b) FTIR spectra of GO-Or and RGO-M40.

The area under the CV curve of RGO-M40 is quite smaller than RGO-MP40, but is slightly superior to GO-Or, indicating the poor electrochemical performance of RGO-M40. The FTIR spectra of RGO-M40 shows that a large amount of oxygen functional groups remained on the surface of RGO-M40. Therefore, we can conclude that microwave has little reduction effect on GO. The poor electrochemical performance and the remaining of large amount of functional groups are due to the low treatment temperature which did not exceed 100 °C.

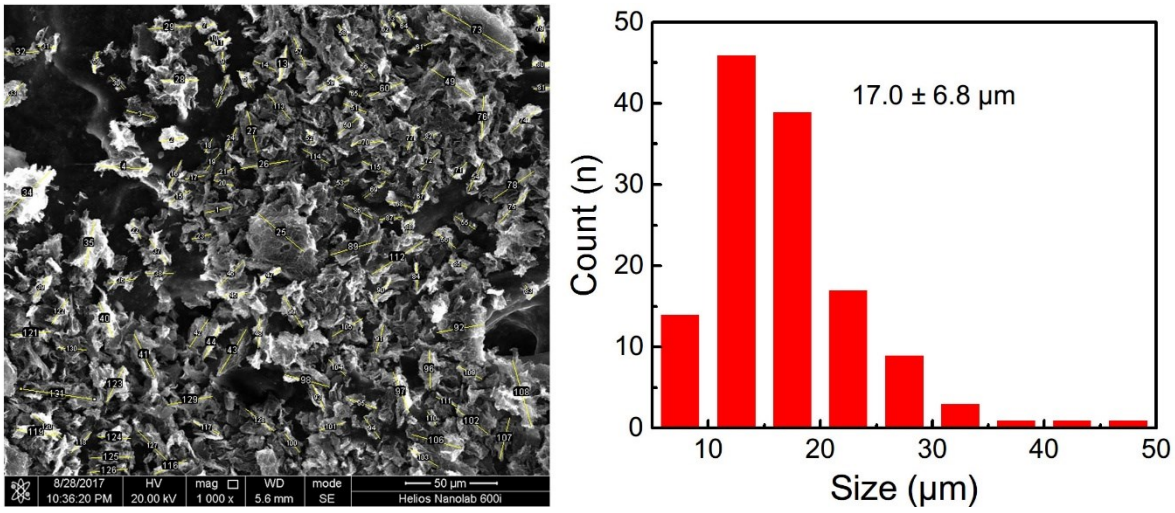

Figure S4 The lateral size distribution of the RGO-MP40 graphene powder.

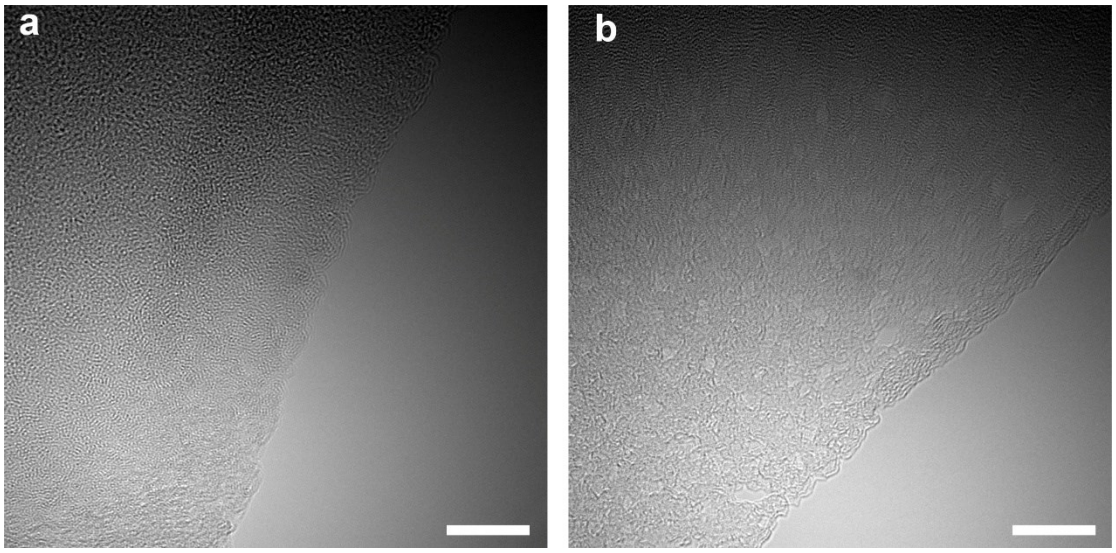

Figure S5 TEM of (**a**) RGO-MP40 and (**b**) RGO-H40. Scale bar, 10μm.

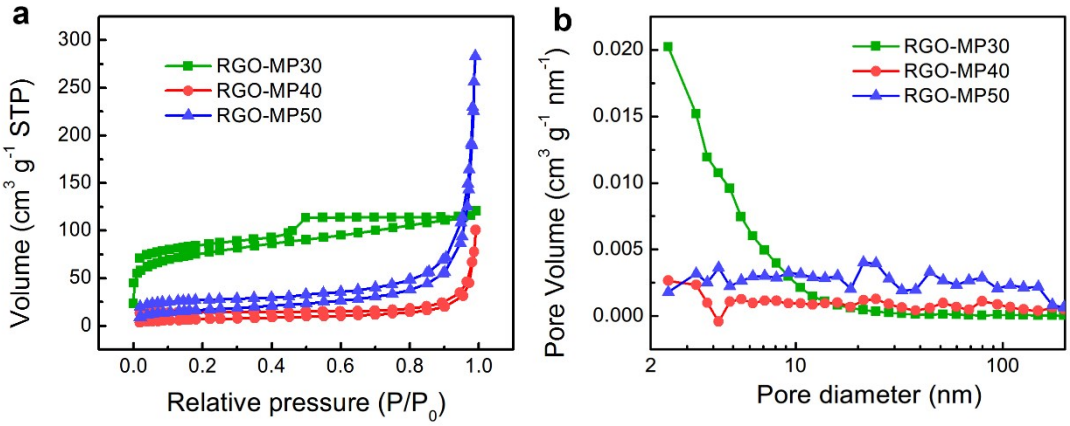

Figure S6 (**a**) N_2 sorption isotherms and (**b**) corresponding pore size distribution.

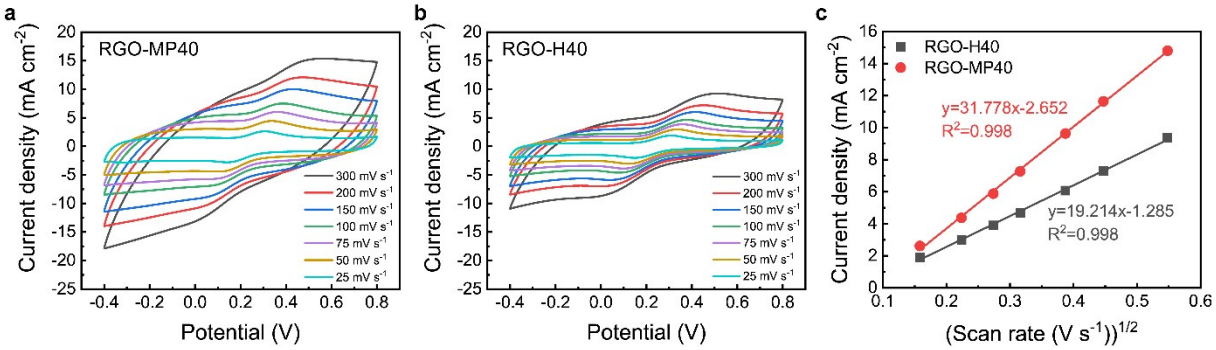

Figure S7 Cyclic voltammograms of (a) RGO-MP40 and (b) RGO-H40 in a 10 mM $[Fe(CN)_6]^{3-/4-}$ and 0.1 M KCl solution at different scan rates from 25 to 300 mV s^{-1}. (c) Peak currents as a function of scan rate for the determination of the effective surface area.

The peak current i_p and the square root of scan rate v are in good linear relationships for both RGO-MP40 (slope = 31.778) and RGO-H40 (slope = 19.214). The active surface area of RGO-MP40 and RGO-H40 are calculated to be 0.954 m^2 g^{-1} and 0.577 m^2 g^{-1}, respectively, indicating the higher electrolyte accessible surface area of RGO-MP40 than that of RGO-H40. But those active surface areas are much lower than those measured by BET method. This may be ascribed to some limitations of this method:

(1) The Randles–Sevcik equation is strictly valid only for linear diffusion at a plane electrode [18]. In porous electrode, the electrolyte ions are restricted in the narrow spaces inside the electrode, unsatisfying the linear diffusion condition. In addition, the diffusion coefficient D would decrease greatly nearby the electrode surface or inside the micropores, leading to the underestimation of the peak current. (2) The local concentration of $Fe(CN)_6^{3-/4-}$ would be changed due to the specific adsorption on the electrode surface. (3) The diameter of the hydrated $Fe(CN)_6^{3-/4-}$ is 0.76~1.34 nm [19], much larger than the interlayer spacing of RGOs (0.35~0.37 nm), thus it cannot probe the surface area between two individual graphene layers. In summary, this method is not so suitable for effective surface area determination to be used in our systems.

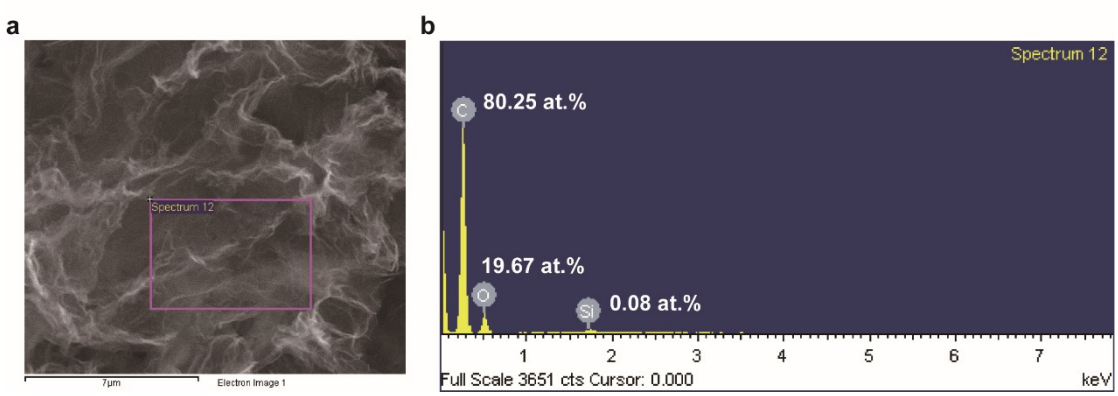

Figure S8 Energy-Dispersive X-ray Spectrometry (EDS) spectrum of RGO-MP40. (a) SEM image of RGO-MP40. (b) The EDS spectrum signal. There is no P signal, indicating there is no residual H_3PO_4. The trace amount of Si element might come from the quartz beaker, which served as the container.

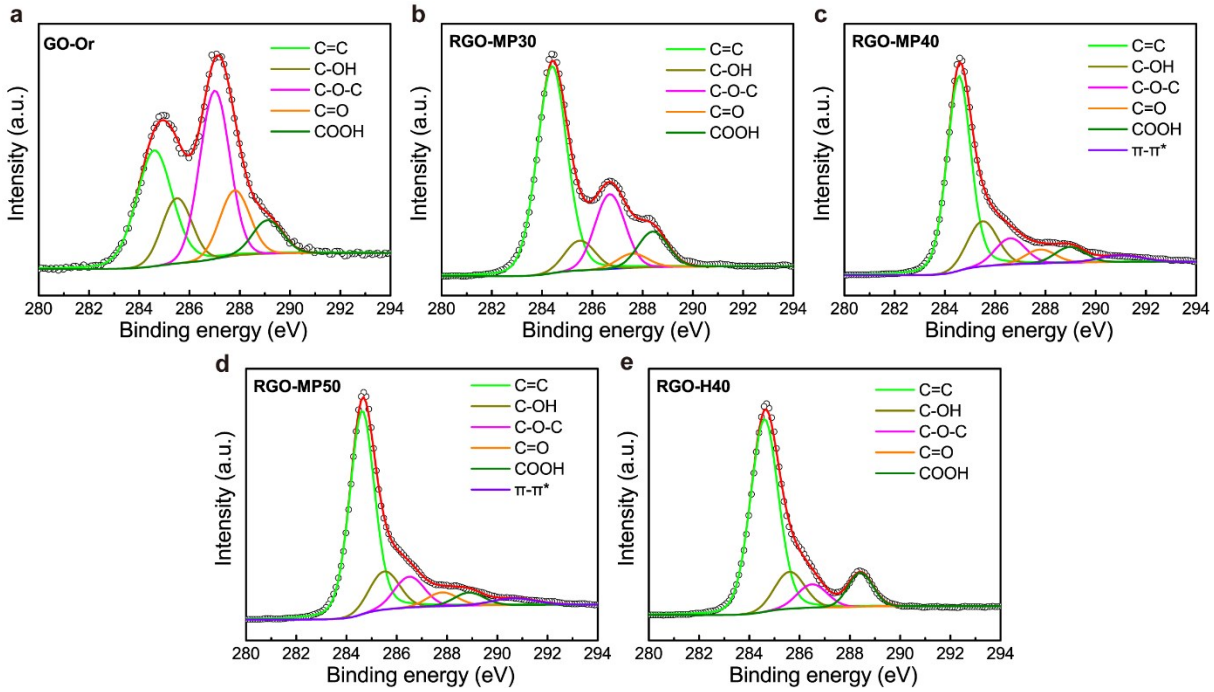

Figure S9 High-resolution of C1s spectra of (a) GO-Or, (b) RGO-MP30, (c) RGO-MP40, (d) RGO-MP50, and (e) RGO-H40, respectively.

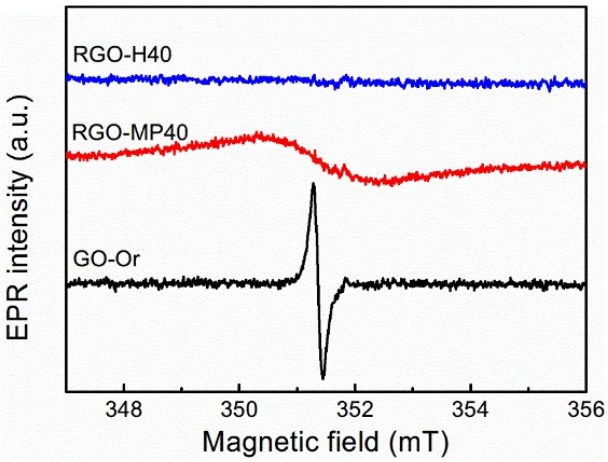

Figure S10 EPR spectra for GO-Or, RGO-MP40 and RGO-H40, which exhibit a single signal at g ~2.0035 with symmetric shape for GO-Or and RGO-MP40. The ΔB_{pp} of GO-Or equal to 0.16 mT, while RGO-MP40 has radical signals with a broader line width of 2.2 mT.

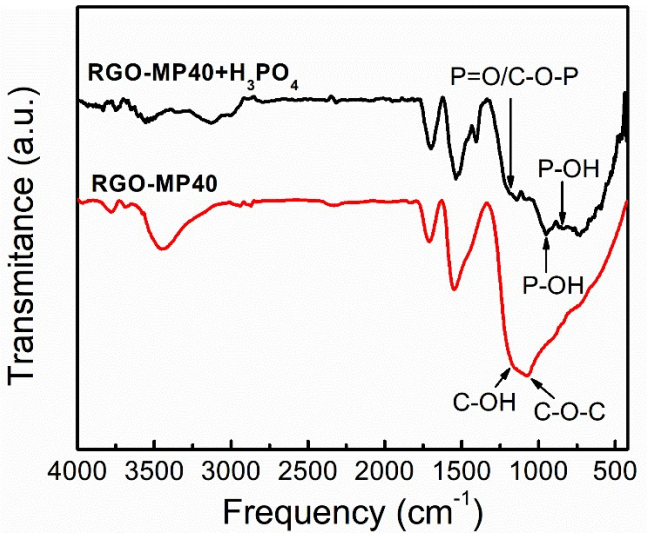

Figure S11 FTIR spectra of RGO-MP40 and RGO-MP40+H_3PO_4.

Preparation of the sample of RGO-MP40+H_3PO_4: The mixture of RGO-MP40 and H_3PO_4 produced from the PAT process (microwave for 40 min) was diluted 500 times with deionized water. The diluted solution was filtered without further washing to ensure remain a small amount of H_3PO_4 on the surface of RGO-MP40. The filtered sample was dried in vacuum oven at 120 °C for 2h. The resulting sample was denoted as RGO-MP4+H_3PO_4.

The presence of the peaks at 1200 cm^{-1} (P=O/C-O-P) and 954 cm^{-1} (P-OH) confirms the formation of phosphoester bond between H_3PO_4 and RGO-MP40 [20-22]. In addition, no signal of P element in XPS and EDS spectra for RGO-MP40 suggested the completely hydrolysis of the C-O-P bond after the washing step. After H_3PO_4 was completely removed (sample RGO-MP40), the vibration intensity of C-OH (~1176 cm^{-1}) significantly increased, indicating the regeneration of C-OH group.

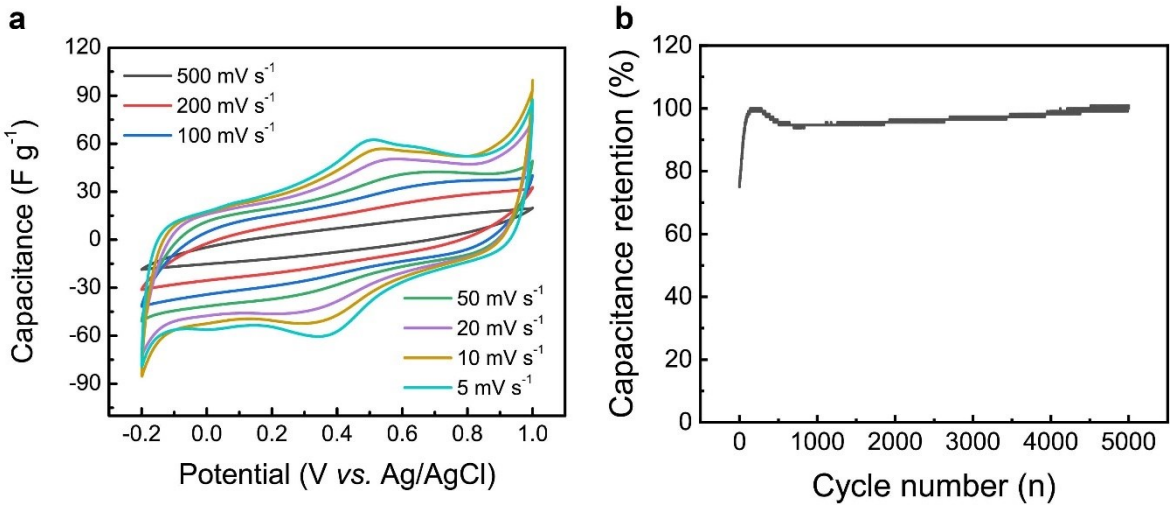

Figure S12 (a) The CV curves of GO-Or at different scan rates. (b) Cycling stability of GO-Or.

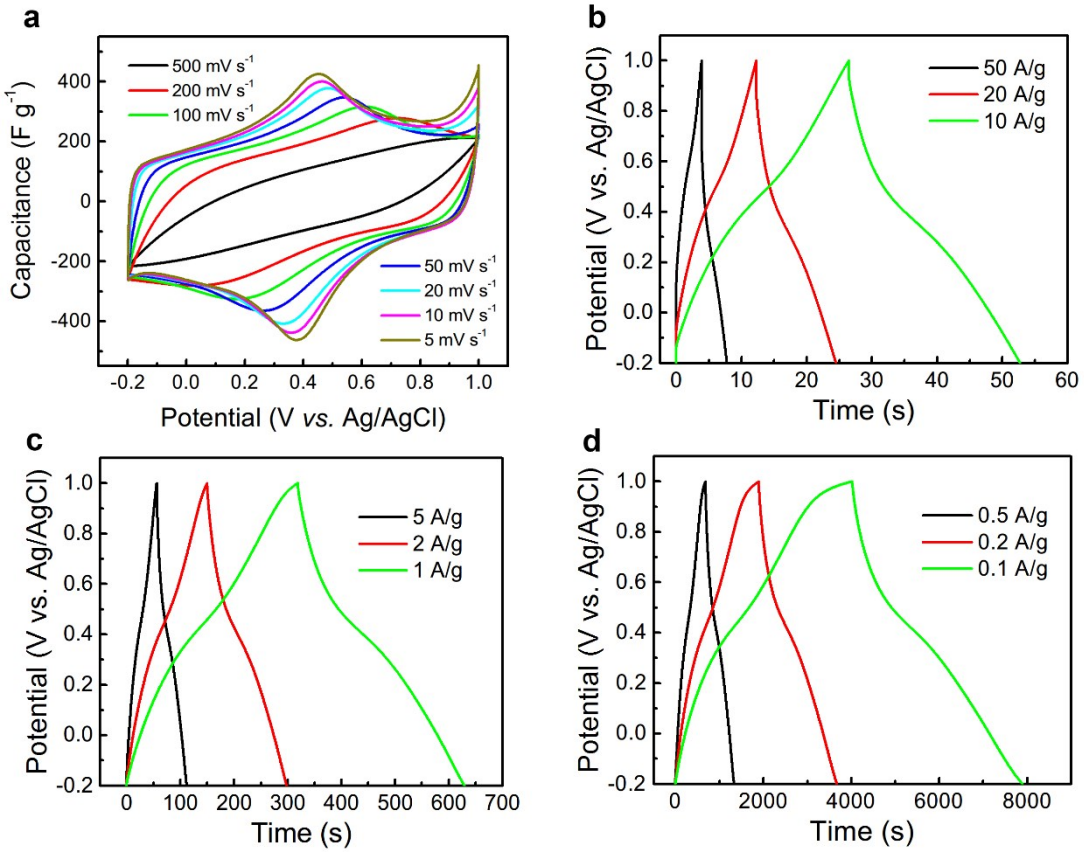

Figure S13 (a) The CV curves of RGO-MP40 at different scan rates. (b-d) The charge/discharge curves of RGO-MP40 at different current densities. Mass loading, 2.5 mg cm^{-2}.

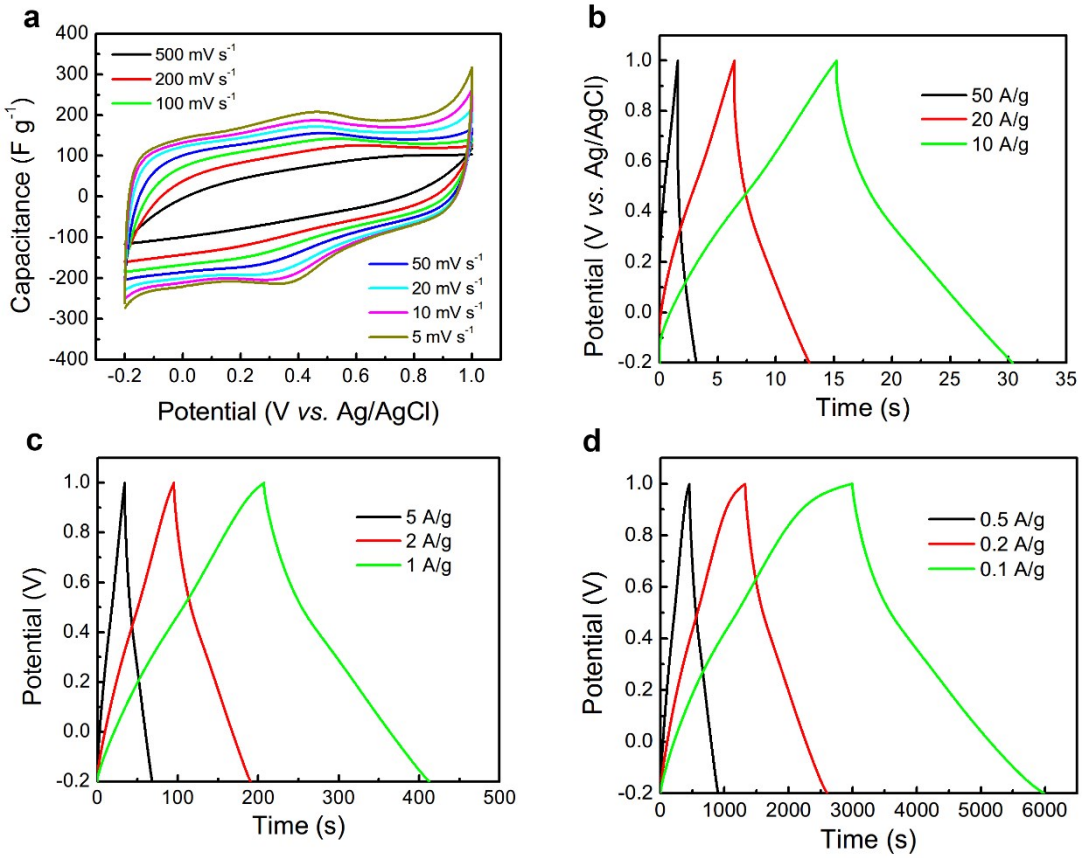

Figure S14 (**a**) The CV curves of RGO-H40 at different scan rates. (**b-d**) The charge/discharge curves of RGO-H40 at different current densities. Mass loading, 2.5 mg cm^{-2}.

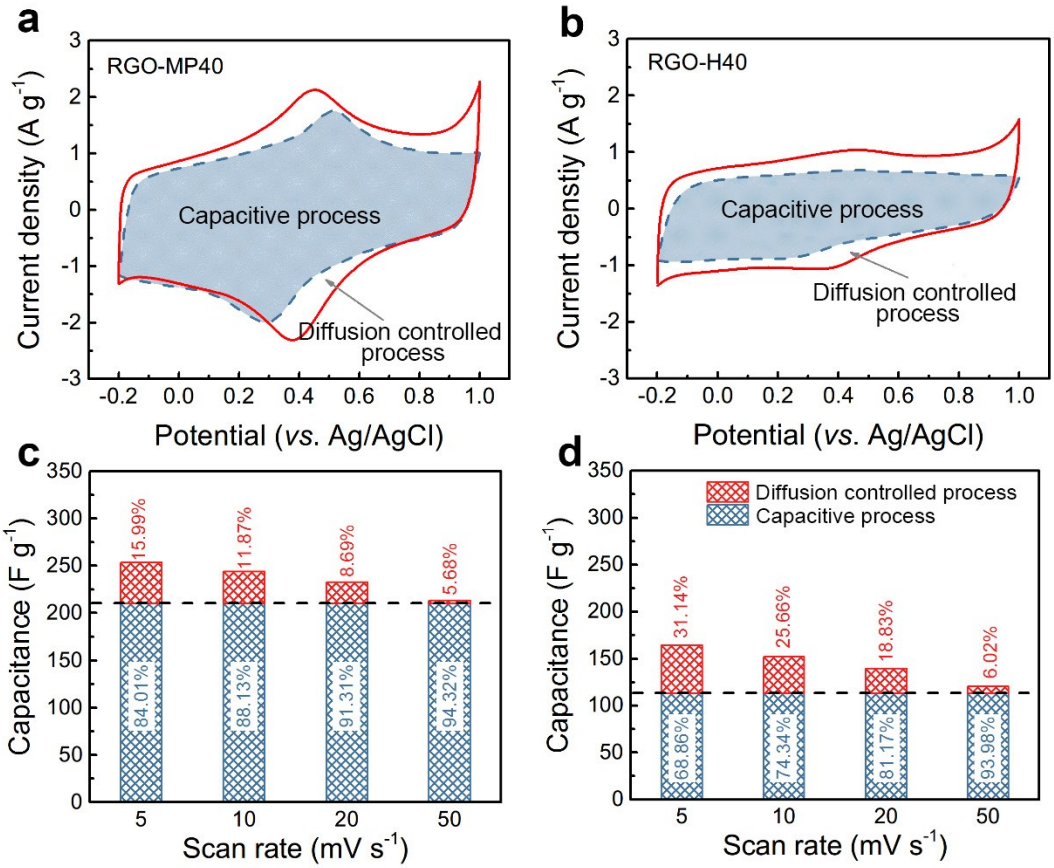

Figure S15 The mechanism of charge storage. Decoupling of the capacitance contributed by capacitive process and diffusion-controlled intercalation process of (**a**) RGO-MP40 and (**b**) RGO-H40. Histograms of the capacitance contributions at different scan rates of (**c**) RGO-MP40 and (**d**) RGO-H40.

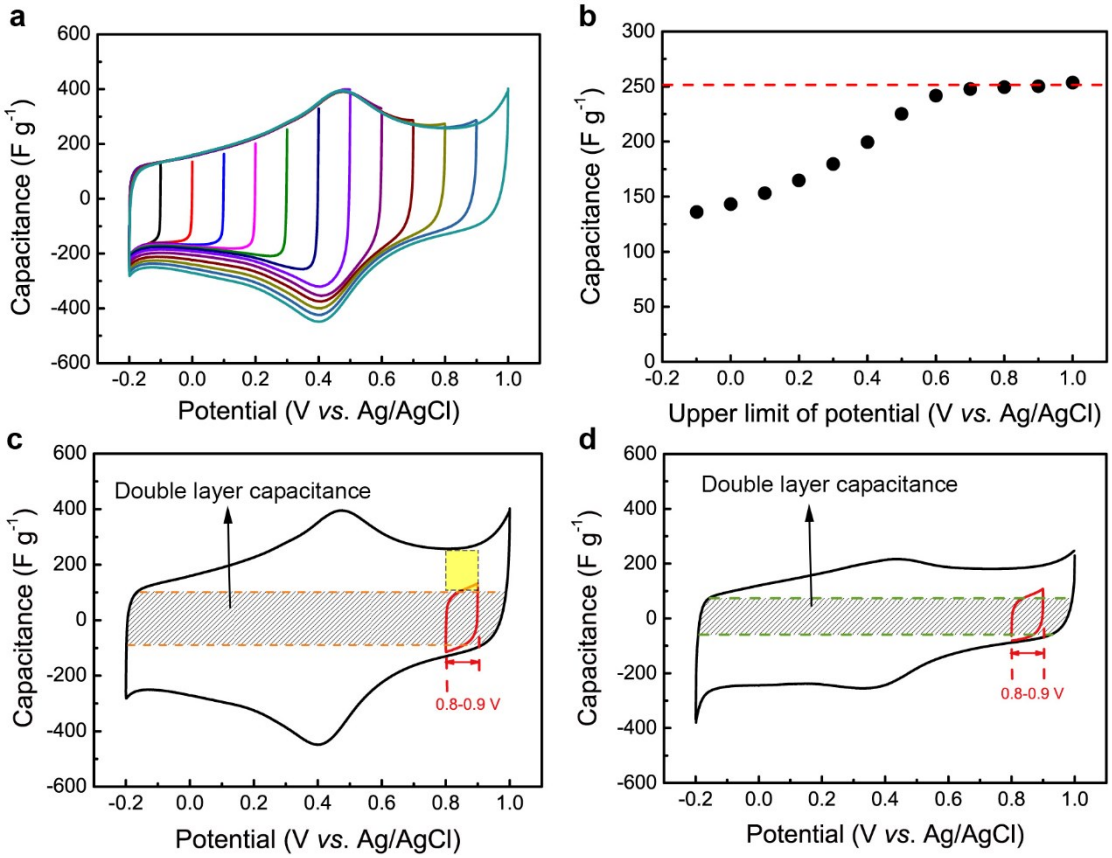

Figure S16 The estimation of the contribution of double layer capacitance (C_{dl}). Scan rate: 5 mV s^{-1}. (**a**) The CV curves of RGO-MP40 at increasing voltage window (from -0.2~-0.1 V to -0.2~1.0 V with a step of 0.1 V). (**b**) Specific capacitance of RGO-MP40 based on the CV curves at increasing upper limit of the potential scan. (**c**) The illustration of C_{dl} of RGO-MP40. The yellow area is related to the faradaic current corresponding to the broaden of redox peaks, commonly observed for redox action controlled by mass transfer. (**d**) The illustration of C_{dl} of RGO-H40. The C_{dl} was calculated from the CV curve tested in the potential range of 0.8~0.9 V.

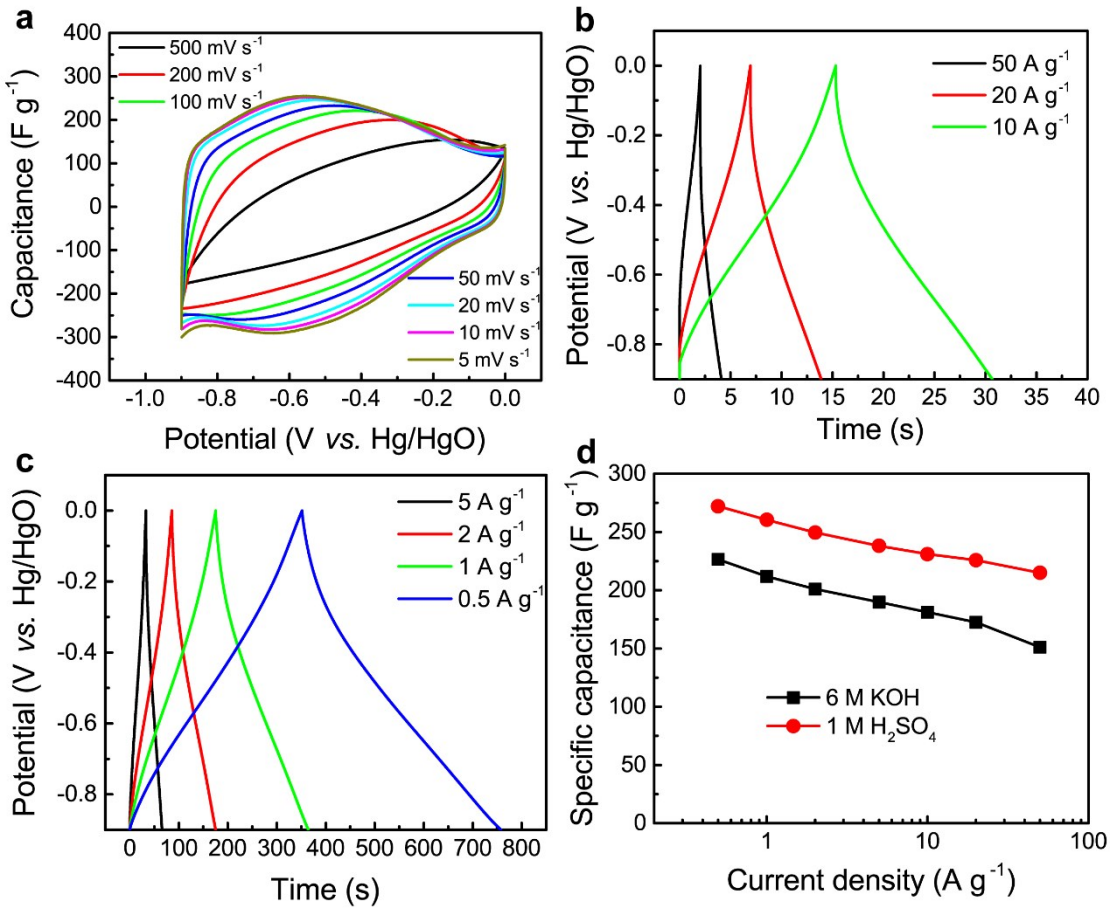

Figure S17 The electrochemical capacitive performance of RGO-MP40 measured in 6 M KOH electrolyte. (**a**) CV curves at various scan rates of 5 to 500 mV s^{-1}. Charge/discharge curves at the current density of (**b**) 10-50 A g^{-1} and (**c**) 0.5-5 A g^{-1}. (**d**) Comparison of the specific capacitances in 6 M KOH and 1 M H_2SO_4 electrolyte at different current densities.

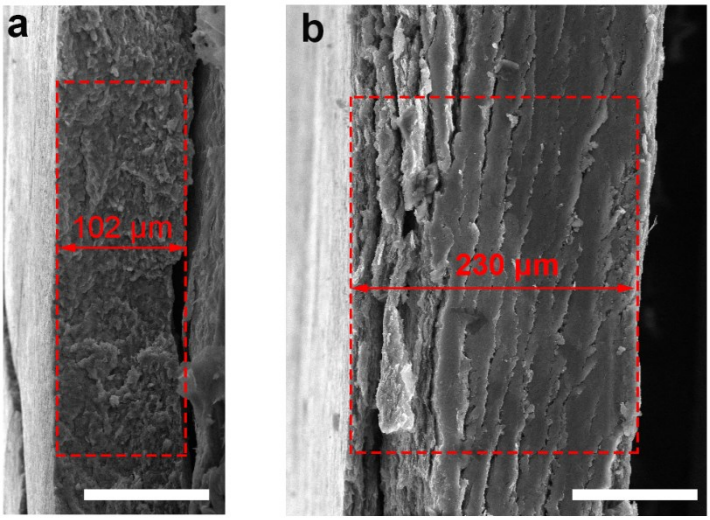

Figure S18 SEM images of cross sections of the obtained electrodes. **(a)** RGO-MP40 and **(b)** RGO-H40. The RGO-MP40 electrode exhibits a continuous, compact and crackless characteristic, which ensure the solid connection between the graphene layers and thus the excellent electric conductivity. As contrast, RGO-H40 electrode with the same mass loading as RGO-MP40 shows an obviously interlaminar crack and loose structure. The total mass (containing active material, carbon black and PVDF) of the electrodes are 15 mg cm^{-2} (the mass loading of active material is 12 mg cm^{-2}), corresponding to $\rho_{electrode}$= 1.47 g cm^{-3} and $\rho_{electrode}$= 0.65 g cm^{-3} for RGO-MP40 and RGO-H40, respectively. The electrode thickness was also measured by the micrometer calipers, which gave the similar results as SEM images. Scale bars: 100 μm.

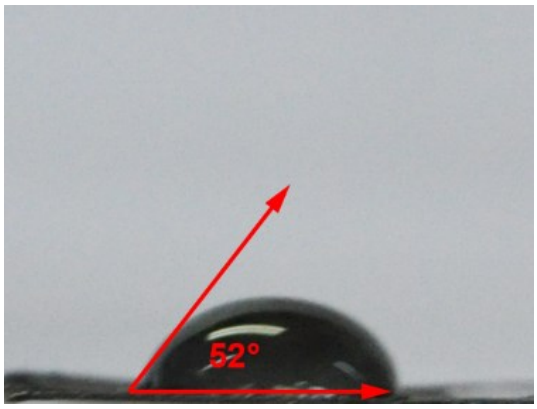

Figure S19 The contact angle of the electrolyte 1 M H_2SO_4 on the surface of RGO-MP40 electrode.

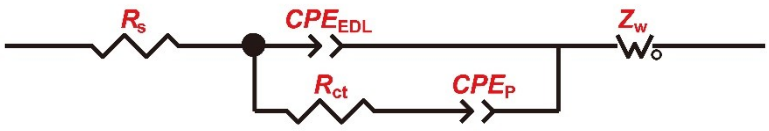

Figure S20 The equivalent electric circuit model used for fitting the Nyquist plots. R_s: the intrinsic ohmic resistance; R_{ct}: charge transfer resistance; CPE_{EDL}: constant phase element representing the electrical double layer capacitance (EDLC); CPE_P: constant phase element representing the pseudocapacitance provided by the oxygen functional groups; Z_w: a Generalized Finite Warburg element terminating in an open circuit.

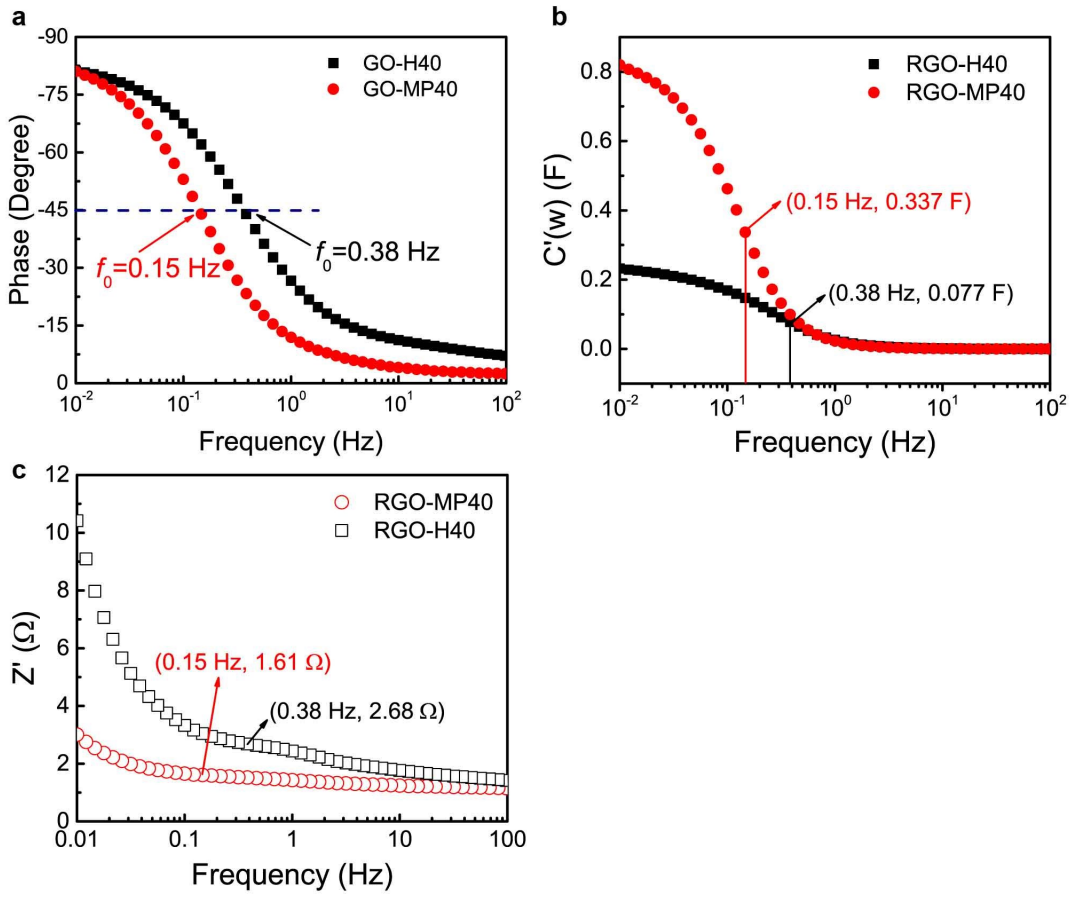

Figure S21 (**a**) Impedance phase angle versus frequency for RGO-MP40 and RGO-H40. The -45° phase angle occurs at ~0.15 Hz for RGO-MP40 and ~0.38 Hz with the RGO-H40. (**b**) Evolution of the real part capacitance *vs.* frequency for the samples of RGO-MP40 and RGO-H40 with a mass loading of 2.5 mg cm^{-2} in the 3-electrode cell. (**c**) Evolution of the real part impedance *vs.* frequency for the sample of RGO-MP40 and RGO-H40 with a mass loading of 2.5 mg cm^{-2} in the 3-electrode cell.

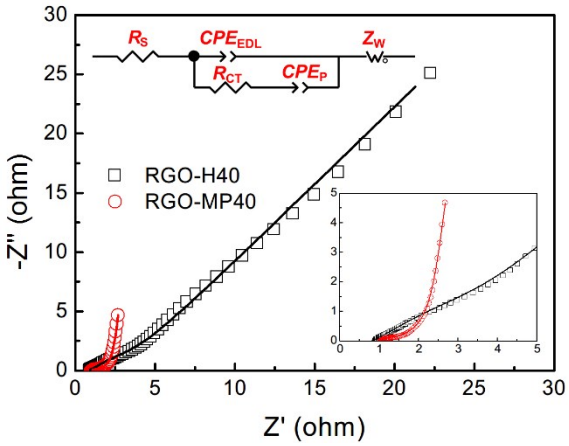

Figure S22 EIS of RGO-MP40 and RGO-H40 with mass loading of 11.9 and 11.5 mg cm^{-2}, respectively. The data were collected at open circuit potentials with 5 mV perturbation and a frequency range of 0.01-100 kHz. The open symbols are experimental data and the solid lines are fitting curves. The bottom inset shows data at high-frequency region and the top inset shows the equivalent circuit.

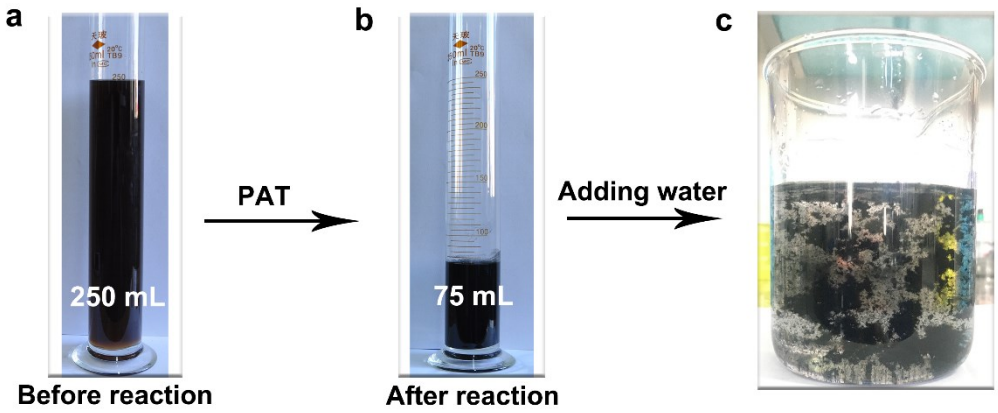

Figure S23 (a) The volume of the mixture of H_3PO_4 and GO before reaction. (b) The volume of the mixture of H3PO4 and GO-MP40 after reaction. (c) The optical photo of RGO-MP40 after adding the mixture in (b) to deionized water.

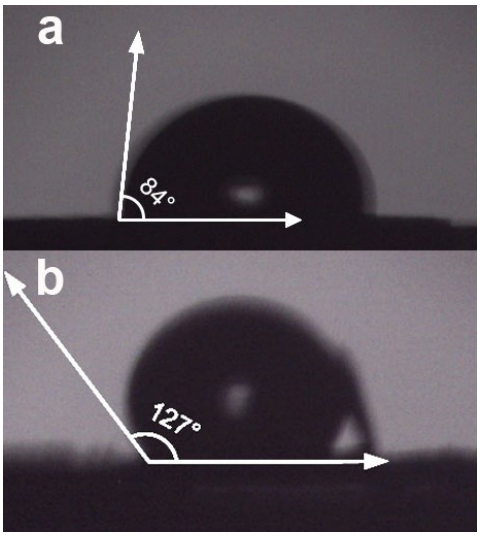

Figure S24 The images of a water drop on the surface of (**a**) RGO-MP40 and (**b**) RGO-H40, respectively.

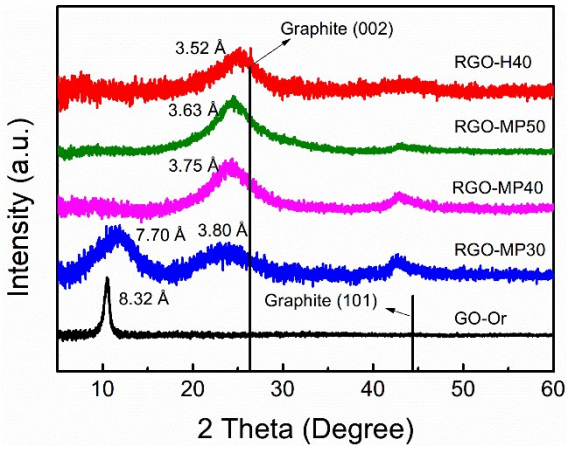

Figure S25 XRD spectra of GO-Or, RGO-MP30, RGO-MP40, RGO-MP50 and RGO-H40.

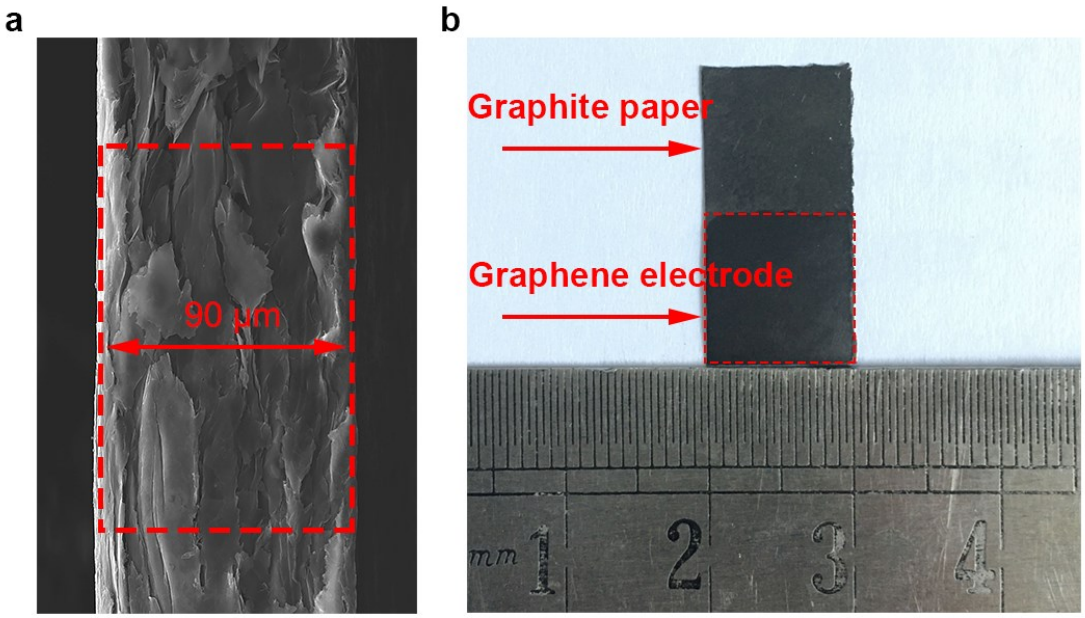

Figure S26 (**a**) The SEM image of the cross section of the graphite paper with a thickness of 90 μm. (**b**) The optical photograph of the graphene electrode RGO-MP40 supported by graphite paper with a mass loading of 2.5 mg cm^{-2}.

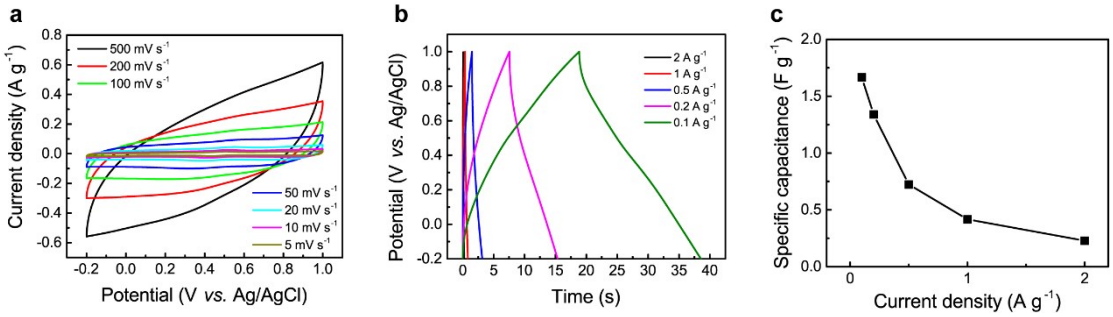

Figure S27 The electrochemical performance of the graphite paper (90 μm in thickness and with an areal density of 17 mg cm^{-2}). (**a**) and (**b**) are the CV and charge/discharge curves of the graphite paper. (**c**) The specific capacitances of the graphite paper at different current densities.

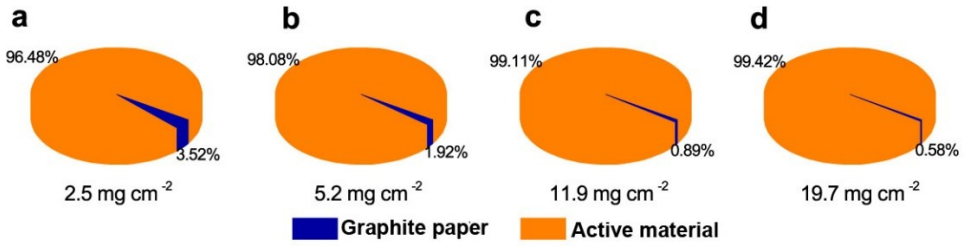

Figure S28 The ratios of the capacitances from the graphite paper and the active material of RGO-MP40 to the total capacitance at different mass loadings.

Table S1 The parameters of specific surface area and total pore volume calculated from nitrogen adsorption measurements.

Samples	BET SSA ($m^2 g^{-1}$)	Total pore volume ($cm^3 g^{-1}$)	Pore size (nm)	Packing density ($g cm^{-3}$)
RGO-MP30	227	0.185	3.26	1.46
RGO-MP40	23	0.146	25.35	1.55
RGO-MP50	56	0.436	31.40	1.07
RGO-H40	198	2.374	48.53	0.35

Table S2 The contents of oxygen functional groups of GO-Or, RGO-MP30, RGO-MP40, RGO-MP50, and RGO-H40 estimated by the XPS area in the C1s peak. (Unit: %)

Samples	C=C	C-OH	C-O-C	C=O	HO-C=O	π-π*
GO-Or	31.5	13.5	34.7	13.5	6.9	0.0
RGO-MP30	59.4	7.9	19.7	3.7	9.4	0.0
RGO-MP40	61.3	15.8	9.2	4.9	5.5	3.3
RGO-MP50	64.3	13.0	10.5	4.7	4.4	3.2
RGO-H40	68.7	13.1	8.2	0.0	9.9	0.0

Table S3 Comparison of the rate capability of RGO-MP40 with other reported carbon-based materials at the same current densities or scan rates.

Materials	Electrolyte	Scan rate or current density	Capacitance (F g^{-1})	Rate capability	Reference
CNC700	1M H_2SO_4	0.1 A g^{-1}	260	43% @ 100 A g^{-1}	[23]
IPGEs	1M H_2SO_4	10 mV s^{-1}	132	36% @ 500 mV s^{-1}	[24]
HCP	1M H_2SO_4	1 A g^{-1}	140	40% @ 64 A g^{-1}	[25]
PrGO-IL	1M H_2SO_4	0.5 A g^{-1}	262	67% @ 20 A g^{-1}	[26]
FG1.3	1M H_2SO_4	1 A g^{-1}	279	54% @ 100 A g^{-1}	[27]
aGA-0.5	1M H_2SO_4	0.2 A g^{-1}	204	69% @ 30 A g^{-1}	[28]
RGO-MP40	1M H_2SO_4	0.1 A g^{-1}	312	66% @ 50 A g^{-1}	**This work**

Table S4 The resistance values obtained from the fitting result. (Unit: Ohm)

	RGO-MP40	RGO-H40
R_s	1.02	1.03
R_{ct}	0.10	0.21
Z_w	0.90	2.92

Table S5 The electrochemical performance of representative carbon electrodes.

[Previous reports without mass loading information are not included. To meet the requirement of practical applications, in general the mass loading of the active materials must be > 5 mg cm^{-2}, and the mass loading of commercialized active carbon electrodes is ~10 mg cm^{-2}.[29] This table by no means is exhaustive but represents the state-of-the-art for comparison. The gravimetric capacitance is calculated based on the active material mass; $C_{V\text{-}m}$: the volumetric capacitance of the active material; $C_{V\text{-}e}$: the volumetric capacitance of the electrode.]

Material	Mass loading (mg cm^{-2})	Packing density (g cm^{-3})	Current density	Gravimetric capacitance (F g^{-1})	Volumetric capacitance (F cm^{-3})	Areal capacitance (mF cm^{-2})	Electrode configuration	Electrolyte	Reference
RGO-MP40	2.5		0.1 A g^{-1}	312	482 ($C_{V\text{-}m}$) 390 ($C_{V\text{-}e}$)	780	3 electrode	1 M H_2SO_4	This work
	11.9	1.55 (ρ_m) 1.47 (ρ_e)	0.1 A g^{-1}	267	414 ($C_{V\text{-}m}$) 314 ($C_{V\text{-}e}$)	3177	3 electrode	1 M H_2SO_4	This work
	19.7		0.1 A g^{-1}	248	384 ($C_{V\text{-}m}$) 292 ($C_{V\text{-}e}$)	4886	3 electrode	1 M H_2SO_4	This work
3D carbon composite	56.9	0.256	10 mV s^{-1}	161	41.3	9160	3 electrode	6 M KOH	[30]
N-doped graphene film	0.32	1.64	1 A g^{-1}	252	413	80.6	2 electrode	1 M H_2SO_4	[31]
	11.2	1.64	1 A g^{-1}	226	370	2531	2 electrode	1 M H_2SO_4	
rGO/SWCNT film	6.2	1.59	114 mA cm^{-3}	255	407	933	2 electrode	H2SO4/PVA	[32]
Multilayered-folded graphene nanoribbon film	21	0.92	5 mA cm^{-2}	318	293	6700	3 electrode	6 M KOH	[33]
Activated wood carbon	30	0.38	1 mA cm^{-2}	118.7	44.8	3204	3 electrode	1 M Na_2SO_4	[34]
Activated Carbon/Graphene Hybrid Aerogels	~10	0.58	0.05 A g^{-1}	294	170.5	2940	2 electrode	6 M KOH	[35]
N- and O-enriched porous carbon/graphene composites	3	0.47	0.1 A g^{-1}	380	178	1140	2 electrode	6 M KOH	[36]

Nitrogen-Doped Mesoporous Carbons	4.0	1.36	0.1 A g^{-1}	147	200	588	2 electrode	1 M H_2SO_4	[37]
carbon/graphene nanofibers@graphene composite cloth	3	1.2	0.2 A g^{-1}	241	294	723	3 electrode	6 M KOH	[38]
nitrogen-enriched porous carbon/graphene	3	1.08	0.05 A g^{-1}	339	365	1017	2 electrode	6 M KOH	[39]
Nitrogen-doped graphene	2.0	1.31	0.5 A g^{-1}	334	437.5	668	3 electrode	6 M KOH	[40]
nitrogen doped holey graphene	2.0	1.30	0.1 A g^{-1}	375	439	750	3 electrode	6 M KOH	[41]
graphene films	0.8	1.6	1 A g^{-1}	340	326	272	3 electrode	1 M H_2SO_4	[42]
	2.84	0.11	1 A g^{-1}	213	25.41	605	3 electrode	1 M H_2SO_4	
nitrogen-doped active carbon/ graphene composites	3	0.68	0.05 A g^{-1}	378.9	257.7	1137	3 electrode	6 M KOH	[43]
Reduced Graphene Oxide Hydrogels	1.92	1.32	1 A g^{-1}	133.7	176.5	257	2 electrode	6 M KOH	[44]
carbon quantum dots	5.16	1.23	0.5 A g^{-1}	128	157.4	660	2 electrode	6 M KOH	[45]
holey reduced graphene oxide	1.5	0.86	1 A g^{-1}	251	216	376.5	3 electrode	6 M KOH	[46]
holey graphene oxide	1.0	1.12	1 A g^{-1}	209	234	209	2 electrode	1 M H_2SO_4	[47]
Functional Pillared Graphene Frameworks	2	1.5	2 mV s^{-1}	353	400	706	3 electrode	6 M KOH	[48]
carbon hollow submicron spheres	0.2	0.87	0.2 A g^{-1}	386	335	77.2	3 electrode	6 M KOH	[49]
graphene nanomesh-carbon nanotube hybrid film	0.5	1.13	5 mV s^{-1}	294	331	147	3 electrode	6 M KOH	[50]
Holey graphene frameworks	1	0.71	1 A g^{-1}	310	220	310	2 electrode	6 M KOH	[51]
Crumpled graphene balls	20	0.5	0.1 A g^{-1}	150	75	3000	2 electrode	5 M KOH	[52]
Liquid-mediated	1	1.33	0.1 A g^{-1}	191.7	255.5	191.7	2 electrode	1 M H_2SO_4	[53]

chemically converted graphene	1	1.33	0.1 A g^{-1}	196.5	261.3	196.5	2 electrode	$EMIMBF_4$/AN	
Liquid-mediated chemically converted graphene	10	1.25	0.1 A g^{-1}	164	205	1640	2 electrode	$EMIMBF_4$/AN	
reduced graphene oxide fiber fabrics	9	0.41	1 mA cm^{-2}	285	117	2812	3 electrode	1 M H_2SO_4	[54]
EGM-rGO film	15	0.94	1 A g^{-1}	201	189	3015	2 electrode	$EMIMBF_4$	[55]
highly ordered and compact porous carbon	2	1.48	0.1 A g^{-1}	255	378	510	3 electrode	1 M $ZnSO_4$	[56]

Supplementary References

1. D. C. Marcano, D. V. Kosynkin, J. M. Berlin, A. Sinitskii, Z. Sun, A. Slesarev, L. B. Alemany, W. Lu and J. M. Tour, *ACS Nano*, 2010, **4**, 4806-4814.
2. F. Yue, G. Gao, F. Li, Y. Zheng and S. Hou, *Carbon*, 2018, **134**, 112-122.
3. J. Yan, Q. Wang, T. Wei, L. L. Jiang, M. L. Zhang, X. Y. Jing and Z. J. Fan, *Acs Nano*, 2014, **8**, 4720-4729.
4. A. Eckmann, A. Felten, A. Mishchenko, L. Britnell, R. Krupke, K. S. Novoselov and C. Casiraghi, *Nano Lett.*, 2012, **12**, 3925-3930.
5. R. Larciprete, S. Fabris, T. Sun, P. Lacovig, A. Baraldi and S. Lizzit, *J. Am. Chem. Soc.*, 2011, **133**, 17315-17321.
6. A. Bagri, C. Mattevi, M. Acik, Y. J. Chabal, M. Chhowalla and V. B. Shenoy, *Nat. Chem.*, 2010, **2**, 581-587.
7. H.-L. Girard, H. Wang, A. d'Entremont and L. Pilon, *The Journal of Physical Chemistry C*, 2015, **119**, 11349-11361.
8. C. Costentin, T. R. Porter and J. M. Saveant, *ACS Appl Mater Interfaces*, 2017, **9**, 8649-8658.
9. H.-L. Girard, B. Dunn and L. Pilon, *Electrochim. Acta*, 2016, **211**, 420-429.
10. L. G. Austin and E. G. Gagnon, *J. Electrochem. Soc.*, 1973, **120**, 251.
11. E. G. Gagnon, *J. Electrochem. Soc.*, 1974, **121**, 512.
12. E. G. Gagnon, *J. Electrochem. Soc.*, 1975, **122**, 521.
13. E. G. Gagnon, *J. Appl. Electrochem.*, 1976, **6**, 95-98.
14. H. A. Andreas and B. E. Conway, *Electrochim. Acta*, 2006, **51**, 6510-6520.
15. K. Brezesinski, J. Wang, J. Haetge, C. Reitz, S. O. Steinmueller, S. H. Tolbert, B. M. Smarsly, B. Dunn and T. Brezesinski, *J. Am. Chem. Soc.*, 2010, **132**, 6982-6990.
16. T. J. Rabbow and A. H. Whitehead, *Carbon*, 2017, **111**, 782-788.
17. V. Augustyn, P. Simon and B. Dunn, *Energ. Environ. Sci.*, 2014, **7**, 1597.
18. S. Trasatti and O. A. Petrii, *J. Electroanal. Chem.*, 1992, **327**, 353-376.
19. M. J. DiTucci and E. R. Williams, *Chem Sci*, 2017, **8**, 1391-1399.
20. M. A. Patel, F. Luo, M. R. Khoshi, E. Rabie, Q. Zhang, C. R. Flach, R. Mendelsohn, E. Garfunkel, M. Szostak and H. He, *ACS Nano*, 2016, **10**, 2305-2315.
21. A. M. Puziy, O. I. Poddubnaya, A. Martinez-Alonso, F. Suarez-Garcia and J. M. D. Tascon, *Carbon*, 2002, **40**, 1493-1505.
22. A. M. Puziy, O. I. Poddubnaya, A. Martinez-Alonso, F. Suarez-Garcia and J. M. D. Tascon, *Carbon*, 2005,

43, 2857-2868.

23. K. Xie, X. T. Qin, X. Z. Wang, Y. N. Wang, H. S. Tao, Q. Wu, L. J. Yang and Z. Hu, *Adv. Mater.*, 2012, **24**, 347-352.
24. L. T. Le, M. H. Ervin, H. W. Qiu, B. E. Fuchs and W. Y. Lee, *Electrochem. Commun.*, 2011, **13**, 355-358.
25. D. Salinas-Torres, R. Ruiz-Rosas, M. J. Valero-Romero, J. Rodriguez-Mirasol, T. Cordero, E. Morallon and D. Cazorla-Amoros, *J. Power Sources*, 2016, **326**, 641-651.
26. T. T. Li, N. Li, J. W. Liu, K. Cai, M. F. Foda, X. M. Lei and H. Y. Han, *Nanoscale*, 2015, **7**, 659-669.
27. F. Liu and D. F. Xue, *Chem. Eur. J.*, 2013, **19**, 10716-10722.
28. X. X. Sun, P. Cheng, H. J. Wang, H. Xu, L. Q. Dang, Z. H. Liu and Z. B. Lei, *Carbon*, 2015, **92**, 1-10.
29. A. Balducci, D. Belanger, T. Brousse, J. W. Long and W. Sugimoto, *J. Electrochem. Soc.*, 2017, **164**, A1487-A1488.
30. T. T. Gao, Z. Zhou, J. Y. Yu, J. Zhao, G. L. Wang, D. X. Cao, B. Ding and Y. J. Li, *Adv. Energy Mater.*, 2019, **9**, 1802578.
31. T. Q. Huang, X. Y. Chu, S. Y. Cai, Q. Y. Yang, H. Chen, Y. J. Liu, K. Gopalsamy, Z. Xu, W. W. Gao and C. Gao, *Energy Storage Materials*, 2019, **17**, 349-357.
32. J. Zhong, W. Sun, Q. Wei, X. Qian, H. M. Cheng and W. Ren, *Nat Commun*, 2018, **9**, 3484.
33. L. Sheng, J. Chang, L. Jiang, Z. Jiang, Z. Liu, T. Wei and Z. Fan, *Adv. Funct. Mater.*, 2018, DOI: 10.1002/adfm.201800597, 1800597.
34. C. Chen, Y. Zhang, Y. Li, J. Dai, J. Song, Y. Yao, Y. Gong, I. Kierzewski, J. Xie and L. Hu, *Energ. Environ. Sci.*, 2017, **10**, 538-545.
35. Q. Z. Zhu, L. Ma, H. R. Wang, M. Q. Jia, Y. B. Guan and B. Xu, *Chemistryselect*, 2017, **2**, 4456-4461.
36. S. W. Zhou, Q. X. Xie, S. H. Wu, X. L. Huang and P. Zhao, *Ionics*, 2017, **23**, 1499-1507.
37. X. Q. Yang, H. Ma and G. Q. Zhang, *Langmuir*, 2017, **33**, 3975-3981.
38. Q. X. Xie, S. W. Zhou, S. H. Wu, Y. F. Zhang and P. Zhao, *Appl. Surf. Sci.*, 2017, **407**, 36-43.
39. Q. X. Xie, G. H. Chen, R. R. Bao, Y. F. Zhang and S. H. Wu, *Micropor. Mesopor. Mater.*, 2017, **239**, 130-137.
40. X. Zhao, H. W. Dong, Y. Xiao, H. Hu, Y. J. Cai, Y. R. Liang, L. Y. Sun, Y. L. Liu and M. T. Zheng, *Electrochim. Acta*, 2016, **218**, 32-40.
41. Y. J. Zhang, L. Ji, W. F. Li, Z. Zhang, L. Lu, L. S. Zhou, J. H. Liu, Y. Chen, L. W. Liu, W. Chen and Y. G. Zhang, *J. Power Sources*, 2016, **334**, 104-111.

42. L. L. Zhang, C. Yang, N. T. Hu, Z. Yang, H. Wei, C. X. Chen, L. M. Wei, Z. C. J. Xu and Y. F. Zhang, *Nano Energy*, 2016, **26**, 668-676.

43. Q. X. Xie, R. R. Bao, A. R. Zheng, Y. F. Zhang, S. H. Wu, C. Xie and P. Zhao, *ACS Sustain. Chem. Eng.*, 2016, **4**, 1422-1430.

44. V. H. Pham and J. H. Dickerson, *J. Phys. Chem. C*, 2016, **120**, 5353-5360.

45. G. X. Chen, S. L. Wu, L. W. Hui, Y. Zhao, J. L. Ye, Z. Q. Tan, W. C. Zeng, Z. C. Tao, L. H. Yang and Y. W. Zhu, *Sci. Rep.-UK*, 2016, **6**, 19028.

46. Y. L. Bai, X. F. Yang, Y. B. He, J. Y. Zhang, L. P. Kang, H. Xu, F. Shi, Z. B. Lei and Z. H. Liu, *Electrochim. Acta*, 2016, **187**, 543-551.

47. Y. X. Xu, C. Y. Chen, Z. P. Zhao, Z. Y. Lin, C. Lee, X. Xu, C. Wang, Y. Huang, M. I. Shakir and X. F. Duan, *Nano Lett.*, 2015, **15**, 4605-4610.

48. L. L. Jiang, L. Z. Sheng, C. L. Long, T. Wei and Z. J. Fan, *Adv. Energy Mater.*, 2015, **5**, 1500771.

49. D. Y. Guo, X. Chen, Z. P. Fang, Y. F. He, C. Zheng, Z. Yang, K. Q. Yang, Y. Chen and S. M. Huang, *Electrochim. Acta*, 2015, **176**, 207-214.

50. L. Jiang, L. Sheng, C. Long and Z. Fan, *Nano Energy*, 2015, **11**, 471-480.

51. Y. Xu, Z. Lin, X. Zhong, X. Huang, N. O. Weiss, Y. Huang and X. Duan, *Nat. Commun.*, 2014, **5**, 4554.

52. J. Luo, H. D. Jang and J. Huang, *ACS Nano*, 2013, **7**, 1464-1471.

53. X. Yang, C. Cheng, Y. Wang, L. Qiu and D. Li, *Science*, 2013, **341**, 534-537.

54. F. Shao, N. Hu, Y. Su, L. Yao, B. Li, C. Zou, G. Li, C. Zhang, H. Li, Z. Yang and Y. Zhang, *Chem. Eng. J.*, 2020, **392**, 123692.

55. Z. Li, S. Gadipelli, H. Li, C. A. Howard, D. J. L. Brett, P. R. Shearing, Z. Guo, I. P. Parkin and F. Li, *Nat. Energy*, 2020, **5**, 160-168.

56. H. Ma, H. Chen, M. Wu, F. Chi, F. Liu, J. Bai, H. Cheng, C. Li and L. Qu, *Angew. Chem. Int. Ed. Engl.*, 2020, **59**, 2-11.